Journal of the American Ceramic Society

RESEARCH ARTICLE

Reactive Sintering of Oxide Nanoceramic Composites via a Redox-Driven Eutectoid Synthesis Route

Russell A. Maier[1] | James S. Zuback[1] | Lynnora O. Grant-Kahan[2] | Aaron C. Johnston-Peck[1]

[1]Material Measurement Laboratory, National Institute of Standards and Technology, Gaithersburg, Maryland, USA | [2]Mechanical Engineering and Engineering Science, University of North Carolina at Charlotte, Charlotte, North Carolina, USA

Correspondence: Russell A. Maier (russell.maier@nist.gov)

Received: 24 February 2026 | **Revised:** 3 April 2026 | **Accepted:** 10 April 2026

Keywords: alumina | ceria | hardness | nanoceramic | redox

ABSTRACT

A novel reactive sintering method was developed to produce dense ceramics with nanoscale composite microstructures. This method exploits the variable valence state of cerium ions. Compounds that contain cerium cations can undergo oxidation–reduction (redox) reactions depending on the oxygen activity of the processing environment. The perovskite cerium(III) aluminate, $CeAlO_3$, undergoes a eutectoid transformation in oxidizing conditions to form nanoscale lamella of cerium(IV) dioxide, CeO_2, and Al_2O_3. Unlike a typical eutectoid reaction, the redox activity of cerium provides an additional lever of control (oxygen partial pressure) over the onset and kinetics of the eutectoid transformation. Multiple processes that affect the final sintered microstructure (densification, coarsening, and volume expansion) of a ceramic can negatively interact and result in porosity or coarsening. By controlling the oxygen atmosphere during sintering, the rates of these competing processes can be optimized to yield a fine-featured and dense product. Testing indicates that finer CeO_2/Al_2O_3 composite microstructures exhibit improved hardness, and microscopy results indicate that these nano-features introduce crack deflection mechanisms. This reactive sintering method provides a tool to produce bulk ceramics with near-theoretical densities and nanoscale microstructures, a method that may be generalized to other oxide systems that undergo redox-activated eutectoid transformations.

1 | Introduction

Optimizing the sintering (densification) process is one of the most impactful strategies to control the relationship between the microstructure and properties of advanced ceramics [1–3]. An ideal sintering process produces a fully dense (pore-free) structure, retains (or develops) the desired microstructure, and minimizes dimensional changes, as processing routes that reduce the amount of shrinkage during sintering provide improvements to the dimensional tolerance and manufacturability of parts [4–7]. However, the mass transport that is necessary for sintering is frequently in direct competition with these desirable outcomes [8]. Elimination of pores reduces the overall dimensions of the ceramic body, while the thermal energy applied during sintering promotes microstructural coarsening or even phase transformations. As a result, densifying nanoceramics (defined here as ceramic materials with grains, phases, or inclusions with at least one dimension smaller than 100 nm), including those with composite microstructures, poses a difficult challenge. Developing novel methods to produce dense,

This work was recently presented at the International Conference on Advanced Ceramics and Composites in January 2026 (ICACC-S1-016-2026): Novel processing of sub-100 nm CeO_2/Al_2O_3 composite microstructures via a eutectoid reactive sintering route.

fine-featured microstructures is essential because properties and functionalities can improve with decreasing feature size. For example, increased hardness scales with a decrease in grain size, following Hall–Petch behavior [9]. The benefits of engineering finer grain sizes and composite microstructures have been demonstrated for mechanical [10, 11], dielectric [12], optical [13], thermal [14], and multifunctional properties [15].

Existing sintering techniques can address issues related to shrinkage during densification or achieve nanoscale microstructural control, but typically not both [6, 16–22]. Methods that simultaneously preserve nanoscale features, reduce porosity, and mitigate shrinkage during sintering remain sparse [10]. We explore utilizing a phase transformation during the sintering process (an approach referred to as reactive sintering) to address this challenge, where a chemical reaction and densification occur during a singular heat treatment [4, 23–25]. A change in molar volume between the product and reactants creates the opportunity to address shrinkage and facilitate near-net part fabrication. Furthermore, a phase transformation can generate a final microstructure with feature sizes or morphologies distinctly different from the parent. When the chemical reaction or phase transformation is thermally activated, the kinetics of the reaction or phase transformation and the sintering phenomena are then intimately linked. This dynamic of both mechanisms being thermally activated is frequently the case when two or more reactants are mixed together, and it can be difficult to gain sufficient kinetic control of the individual processes to achieve a desirable combination of density and microstructure. For example, if the phase transformation precedes densification, the continuation of the heat treatment needed to eliminate the pores would also facilitate microstructural coarsening [26]. The resulting competition between densification and grain growth mirrors the challenge in traditional sintering, where grain growth that outpaces the kinetics of porosity removal can result in specimens with poor densities. Therefore, for reactive sintering to produce a dense ceramic with nanoscale grains, strict kinetic control over both the phase transformation and sintering processes is needed.

To gain additional control over the kinetics of the reactive sintering process, we explore a phase transformation whose reaction rate can be readily managed using a processing parameter in addition to temperature, namely oxygen activity. Cerium-based oxides are sensitive to oxygen partial pressure in the temperature ranges where sintering is active. Cerium cations can exist in the Ce(III) and Ce(IV) valence states, where the relative stability of the Ce(III) and Ce(IV) valence states depends on the chemical environment [27, 28]. This behavior is exemplified by cerium dioxide, CeO_2, a reducible oxide that can accommodate oxygen lattice vacancies. Reduction/oxidation (redox) reactions (Equations 1 and 2) describe the change in valence state of cerium oxide, where δ indicates the amount of oxygen non-stoichiometry, of which the fluorite phase can accommodate a significant amount of oxygen vacancy point defects. A δ value approaching 0.3 results in transformation of the structure from fluorite to a series of defective phases, Ce(III, IV), and finally to a sesquioxide Ce_2O_3–Ce(III) phase at δ approaching 0.5 [29–31]:

$$\frac{1}{\delta}CeO_2 + H_2 \rightarrow \frac{1}{\delta}CeO_{2-\delta} + H_2O \quad (1)$$

$$\frac{1}{\delta}CeO_{2-\delta} + \frac{1}{2}O_2 \rightarrow \frac{1}{\delta}CeO_2 \quad (2)$$

As expressed in Equations (1) and (2), the oxygen stoichiometry can be controlled by equilibrating the sample in an oxygen-rich or oxygen-poor environment. Moving beyond a binary oxide (i.e., CeO_2) to a ternary oxide introduces additional possibilities to tailor the type of phase transformation as well as the resultant functional properties of the ceramic. It was recently reported that composite microstructures of CeO_2 and Al_2O_3 with interphase spacing on the nanometer scale could be formed in powders through the eutectoid transformation of the perovskite $CeAlO_3$ [32, 33]. The perovskite $CeAlO_3$ forms from cerium and aluminum oxide under reducing conditions and decomposes to cerium and aluminum oxide under sufficiently oxidizing conditions. This peritectoid/eutectoid couple is reversible, and because Al_2O_3 is unreducible with a stable valence state, the phase space is constrained, limiting the potential for production of undesirable phases [34, 35]. Furthermore, this eutectoid decomposition of $CeAlO_3$ results in a significant volume expansion. Taking room-temperature density values of 6.64, 7.13, and 3.99 g/cm^3 for $CeAlO_3$, CeO_2, and α-Al_2O_3, respectively, the theoretical volume expansion is 18%. This large chemical expansion can mitigate shrinkage during sintering.

Here, we present a method to produce nanoscale composite (CeO_2 and Al_2O_3) ceramics by reactive sintering of $CeAlO_3$. Expansion of the mean material lattice constant due to the eutectoid phase transformation counteracts the volume shrinkage caused by sintering. Incorporating a redox-activated eutectoid also provides a crucial extra degree of processing freedom that facilitates the formation of high-density, nanoscale microstructures. A sintering process that can achieve these multiple attributes (volume expansion, chemical reaction, low porosity, and nanoscale microstructure) is rare in ceramics processing, and this strategy may be generalized to other chemistries that exhibit similar phase transformations, enabling the production of ceramics with optimized properties and novel functionalities.

2 | Procedure

Samples were processed through a mixed-oxide solid-state reaction route. CeO_2 (Inframat Advanced Materials*, 99.9%) and Al_2O_3 (Sumitomo AA04, 99.99%) were weighed and mixed using a planetary mill with stabilized zirconia media in ethanol. The dried powders were separated into two batches: one batch was a control to study CeO_2 and Al_2O_3 sintering, and one batch was processed further to produce $CeAlO_3$, the precursor for reactive sintering. The $CeAlO_3$ precursor was calcined at 1300°C for 18 h in a horizontal tube furnace with flowing 95% N_2 and 5% H_2 forming gas. X-ray diffraction confirmed the formation of $CeAlO_3$, and this powder was milled using the previously described milling procedure. The same procedure to make pellets was followed for both compositions. Pellets were formed by first mixing powder with a 2% by mass solution of Acryloid B72 polymer and sieving the binder-modified powder through a 100 mesh. Powders were pressed uniaxially in a 10 mm steel die, followed by isostatic pressing at 200 MPa. Smaller cross-section samples, 5 mm, were also prepared for dilatometry experiments. The samples were pre-fired to burn out the binder to a temperature of 600°C at a rate of

0.5°C/min. These green pellets were weighed and measured to record green density prior to sintering.

Dilatometry experiments were performed on samples that were pre-fired to remove organics. Experiments were performed on a Linseis DIL L75 dilatometer in air or under flowing argon gas. Thermogravimetric analysis (TGA) of $CeAlO_3$ was carried out by heating 30 ± 3 mg of powder in a platinum crucible to 1075°C at a rate of 15°C/min under flowing argon. The mass of these samples was then measured under isothermal conditions in mixed air/argon environments using a Netzsch STA 449 F1 thermogravimetric analyzer. The mixed flow of air and argon gases was controlled using the internal mass flow controllers of the instrument, and the oxygen partial pressure of the outflow gas was measured with a zirconia-based oxygen analyzer (Yokogawa OX400).

Scanning transmission electron microscopy (STEM) samples were prepared from bulk samples using a multisource plasma-focused ion beam (PFIB) dual-beam microscope. A xenon ion beam was used. Initial cuts and thinning were conducted using a 30 keV beam energy, while the final polishing steps used a 5 keV beam energy. High-angle annular dark-field STEM (HAADF STEM) images were acquired using a microscope operated at 300 kV. The convergence semi-angle was approximately 14 mrad, and the detector collection semi-angles were approximately 70–190 mrad. In some cases, a series of images was acquired, aligned by cross correlation [36] and subsequently summed to improve signal to noise and diminish the effect of scan distortions. Selected area electron diffraction (SAED) patterns were acquired using a microscope operated at 300 kV.

For microhardness testing, sintered pellet samples were prepared by cutting each sample in half using a diamond wire saw to produce two equal-sized semicircular cross sections. Samples were first sintered at 1550°C for 12 h under flowing forming gas. A fully CeO_2/Al_2O_3 transformed sample (based on observation of the cross-sectioned microstructure and a recorded gain in mass) was produced by annealing in flowing air at 1550°C for 30 min, followed by quenching the sample by pulling it in a platinum wire basket to a cold end of the tube furnace. The temperature at the cold end of the furnace tube was not monitored, but it was at an elevated temperature due to heat transfer. The samples were then left at the cold end of the tube as the furnace cooled at a programmed rate of 5°C/min. A partially transformed sample (based on observation of the cross-sectioned microstructure and a recorded gain in mass) was produced by heating the sample to 1600°C under flowing forming gas, annealing for 10 min in flowing air, followed by quenching the sample. One sectioned half of each sample was mounted in epoxy, and the cross-sectioned surfaces were polished to a 0.1 μm finish with a diamond slurry suspension. Microhardness testing was performed using a Vickers indenter (NANOVEA CB500) with parameters and analysis guided by ASTM C1327-15. For each indentation, the indenter approached the sample surface at 60 μm/min until a 25 mN contact force was recorded. The sample was then loaded at approximately 196 N/min and held at a target load of 9.81 N (1 kgf) for 10 s before unloading at 100 N/min. A 12-indent by 29-indent map with 136 μm horizontal spacing and 250 μm vertical spacing was used to provide comprehensive mechanical property characterization across the specimen.

The dimensions and mass of sintered samples were measured to calculate the geometric density, and the densities of samples with closed porosity were measured using the Archimedes method. Samples were prepared for scanning electron microscopy (SEM) by polishing to a 1 μm final finish. A combination of diamond-impregnated platens and diamond pastes was used. Prior to sputter coating with carbon, the surfaces of these polished pellets were also analyzed with x-ray diffraction using monochromated Cu-Kα radiation on a PANalytical X'Pert Pro. Polished cross sections of samples were imaged using secondary electrons on a JEOL 7800F FESEM. Effective interlamellar spacings were measured from a total of four SEM micrographs in the vicinity of each microhardness indentation. The micrographs were segmented using a WEKA trainable segmentation algorithm in Fiji [37]. The WEKA approach allows a user to manually paint single-phase regions and use this data as a training classifier that can then be applied to other image files [38]. Batch thresholding of the images was completed in this manner. A modified "Abrams Three-Circle Procedure" described in ASTM E 112–24 was used to algorithmically measure effective interlamellar spacing values (see S12–S14). This measurement was accomplished with a digital, equally spaced, three-concentric-ring image superimposed on each micrograph, where the arc lengths separating Al_2O_3 phase sections were measured for different regions of samples with varying interlamellar spacings (see Supporting Information for additional details).

3 | Results

3.1 | X-ray Diffraction

Select X-ray diffraction patterns of $CeAlO_3$ powder and pellets sintered in oxidizing conditions are shown in Figure 1. The Profex software [39] was used to perform a Rietveld refinement of the powder diffraction profiles using reference patterns PDF# 04-013-4067 ($CeAlO_3$) and PDF# 00-048-0055 ($CeAl_{11}O_{18}$). The slightly lower calcining temperatures used in this study, compared to previous studies where single-phase $CeAlO_3$ has been synthesized [40], led to some secondary CeO_2 phase peaks in the $CeAlO_3$ powder diffraction profile. This choice to reduce the calcine temperature was made to avoid coarsening of the powder to improve the $CeAlO_3$ sinterability. In oxidizing conditions, at temperatures between 1350°C and 1450°C, the $CeAlO_3$ fully decomposes into CeO_2 and α-Al_2O_3. While at temperatures at or above 1550°C, α-Al_2O_3 and CeO_2 continue to react and form the $CeAl_{11}O_{18}$ phase (see Figure S2) [41]. Cerium hexaaluminate ($CeAl_{11}O_{18}$) has been described in previous studies [35, 42–44]; however, this phase was reported to form under different processing conditions (higher temperatures, lower oxygen partial pressures) than those used in the present study. This temperature at which $CeAl_{11}O_{18}$ forms places an upper limit on the sintering temperature for the formation of nano-grained CeO_2/Al_2O_3 microstructures free from $CeAl_{11}O_{18}$ inclusions. However, $CeAl_{11}O_{18}$ inclusions are not necessarily detrimental. $CeAl_{11}O_{18}$ inclusions have been investigated as a strengthening mechanism because of their tendency to form elongated grains

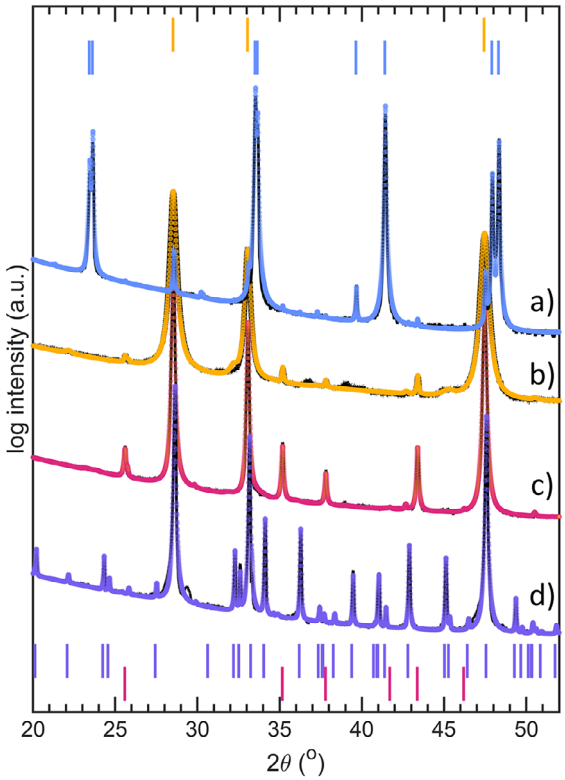

FIGURE 1 | X-ray diffraction (black) of $CeAlO_3$ samples processed under conditions (from top to bottom): (a) annealed at 1350°C under forming gas for 18 h, (b) the surface of a polished pellet sintered at 1200°C in air for 10 min, (c) the surface of a sintered pellet sintered at 1350°C in air for 10 min, and (d) the polished surface of a pellet sintered at 1650°C in air for 20 h. The Rietveld refinements of each spectrum are provided with the tick marks representing the phases (blue) $CeAlO_3$, (yellow) CeO_2, (red) α-Al_2O_3, and (purple) $CeAl_{11}O_{18}$.

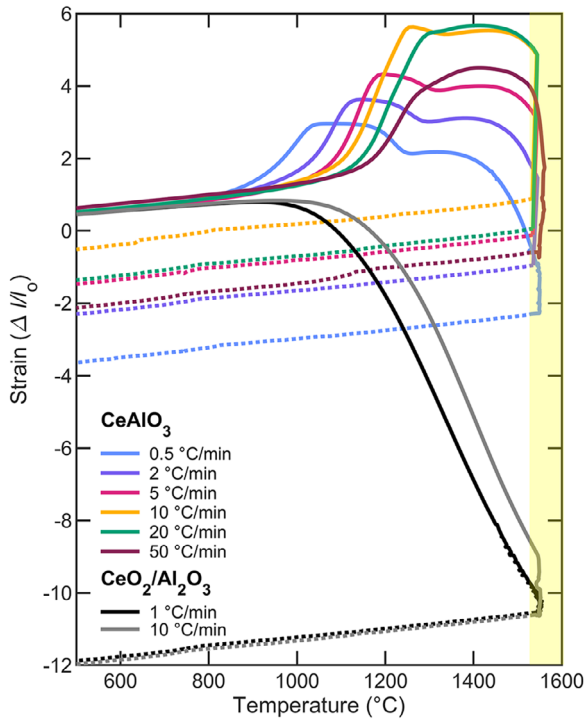

FIGURE 2 | Percent linear strain of samples (both CeO_2/Al_2O_3 and $CeAlO_3$ precursors) heated at constant rates (solid lines) to 1550°C and then held for 1 h (shaded yellow region) followed by cooling (dotted lines). Samples were heated in air. The density of $CeAlO_3$ precursor samples were between 70% and 75% theoretical density while CeO_2/Al_2O_3 precursor samples were approximately 95% theoretical density.

[42], and $CeAl_{11}O_{18}$ inclusions have been shown to improve the toughness of zirconia/alumina ceramic composite materials [45]. Related Sr- and Ca-containing aluminum-rich oxide phases that act as crack-deflecting inclusions [45–51] in toughened ceramics [52] are used in the medical implant field [53, 54].

3.2 | TGA

Kinetics of the eutectoid decomposition, as a function of oxygen concentration, were measured under isothermal conditions at 1075°C. The TGA curves (Figure S1) exhibit a sigmoid shape and approach a value of approximately 3.72%, which is the theoretical increase in mass for the eutectoid decomposition of $CeAlO_3$. Lower oxygen partial pressures significantly slow the reaction, indicating that the kinetics of the eutectoid decomposition are sensitive to oxygen activity. Previous studies demonstrate that temperature also influences the eutectoid reaction rate [32].

3.3 | Dilatometry

3.3.1 | Single-Step Dilatometry

Samples were either sintered using a process that included a single isothermal dwell (sintering temperature) in which the heating step and dwell step were conducted under the same oxygen atmosphere conditions, or samples were sintered using a process that included multiple isothermal dwells and/or were subjected to multiple oxygen atmosphere conditions. To simplify the description of these sintering strategies, heat treatments will be described as single-step or multi-step, going forward. For single-step processing, samples were heated at constant heating rates in air. In Figure 2, linear expansion curves are shown for samples heated at varying rates to 1550°C and held for 1 h before cooling to room temperature at a rate of 20°C/min. The onset of the nonlinear expansion of the sample during heating corresponds to the beginning of the eutectoid decomposition reaction. As discussed in a previous study focused on the kinetics of the decomposition reaction in powdered samples [32], the α-Al_2O_3 phase does not initially form. Rather, the thermodynamically stable corundum phase is preceded by metastable, lower density γ-, δ-, and θ-Al_2O_3 phases before the α-Al_2O_3 phase forms at higher temperatures or longer annealing times (Figure 1), coinciding with observable coarsening of the microstructure from lamellar CeO_2/Al_2O_3 nano-regions to micron-scale equiaxed grains. After the eutectoid reaction results in a maximum expansion of the sample upon heating (Figure 2), the sample exhibits a multi-step contraction. The first contraction that occurs prior to sintering coincides with the temperature range where alumina polymorphs begin to transform to α-Al_2O_3 [32]. This process of transforming lower density polymorphs to α-Al_2O_3 would result in complex mass transport during this portion of the thermal heat treatment [55]. Additional measurements were performed using a mixed CeO_2/Al_2O_3 powder, which does not undergo eutectoid

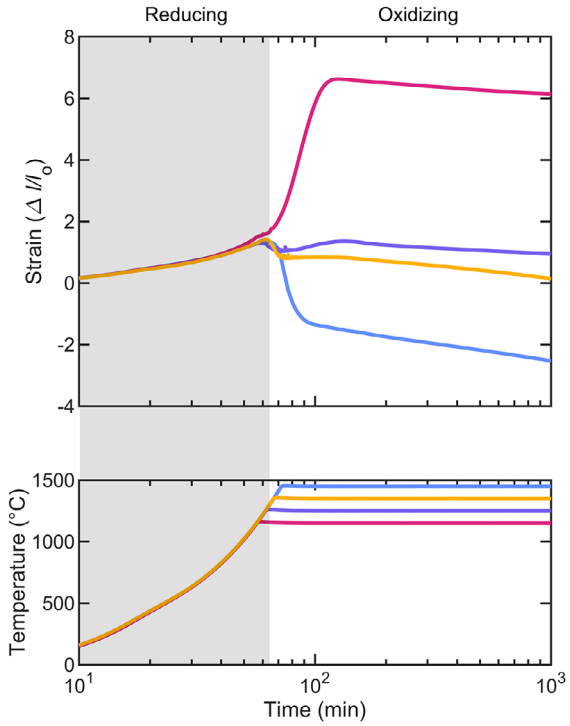

FIGURE 3 | Percent linear strain of $CeAlO_3$ precursor samples heated at a constant rate of 20°C/min to 1150°C, 1250°C, 1350°C, and 1450°C in flowing argon. Once the temperature was reached for the isothermal dwell, the furnace environment was switched from argon (shaded region) to air. The temperature profiles (bottom) correspond to the strain vs. time profile (top) and are color coded to match. Final theoretical densities of the samples were recorded by geometrical method to be 55.8% (red), 64.9% (purple), 66.3% (yellow), and 73.8% (blue). These samples correspond to sample numbers 120624_38, 120624_44, 120624_39, and 120624_48, respectively (see Supporting Information for more details).

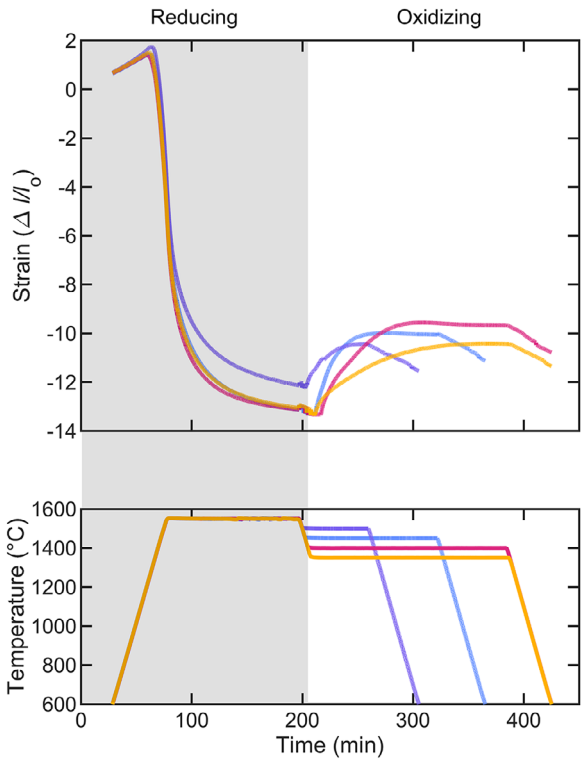

FIGURE 4 | Percent linear strain of $CeAlO_3$ precursor samples heated to 1550°C and held for 2 h under flowing argon. Samples were then cooled under flowing argon to a second isothermal dwell temperature. Upon reaching the second isothermal dwell temperature, the furnace environment was switched from an argon (shaded region) to air atmosphere. The temperature profiles (bottom) correspond to the strain vs. time profile (top) and are color coded to match. Final theoretical densities of the samples were recorded by the Archimedes method to be 98.6% (purple), 98.9% (blue), 98.1% (red), and 94.4% (yellow). These samples correspond to sample numbers 120624_84, 120624_82, 120624_85, and 120624_86, respectively (see Supporting Information for more details).

decomposition and therefore shows no evidence of nonlinear expansion associated with reaction during sintering. The second contraction step occurs at higher temperatures and is indicative of a sintering/pore-removal process. The measurements on the CeO_2/Al_2O_3 powder compacts reveal that shrinkage associated with sintering begins around 1250°C, indicating that sintering mechanisms are simultaneously present in the $CeAlO_3$ compacts as they undergo eutectoid decomposition. Multi-step dilatometry in a controlled atmosphere was essential in decoupling these simultaneous processes.

3.3.2 | Multi-Step Dilatometry

Two types of multi-step heating profiles were used to study the effect of atmosphere on the sintering kinetics of $CeAlO_3$ samples while undergoing a eutectoid decomposition. In one case, samples were heated at a constant heating rate under flowing argon gas to a dwell temperature. Once the dwell temperature was reached, the argon flow was immediately cut off and the sample was exposed to air. The dimensional changes in samples measured using this multi-step process are shown in Figure 3. Samples that were held at temperatures of 1250°C or below upon transitioning from a reducing to an oxidizing environment displayed expansion, while samples heated to temperatures above 1250°C after transitioning from a reducing to an oxidizing atmosphere only registered shrinkage. These datasets show that the kinetics of the volume expansion of the eutectoid decomposition relative to sintering processes that cause shrinkage can be controlled by the oxygen partial pressure as well as the reaction temperature. The samples in Figure 3, measured after the experiment, gained in mass a total of 3.51%, 3.43%, 3.50%, and 3.50% compared to the mass of the starting $CeAlO_3$ sample. This gain in mass is consistent with previous measurements made on fully reacted $CeAlO_3$ material in oxidizing conditions to drive a complete reaction to a CeO_2/Al_2O_3 microstructure [32].

A second heating/oxidation profile was used in which samples were heated at constant heating rates in flowing argon, followed by an isothermal dwell at 1550°C for 2 h. This heating profile promoted densification of the $CeAlO_3$ phase prior to the oxidation-driven reaction. A second isothermal dwell was then conducted at a lower temperature under oxidizing conditions to promote the eutectoid reaction. The dimensional changes of samples measured using this type of multi-step heating/oxidation profile are shown in Figure 4. This sintering profile was developed after observing that samples sintered to near-full density in

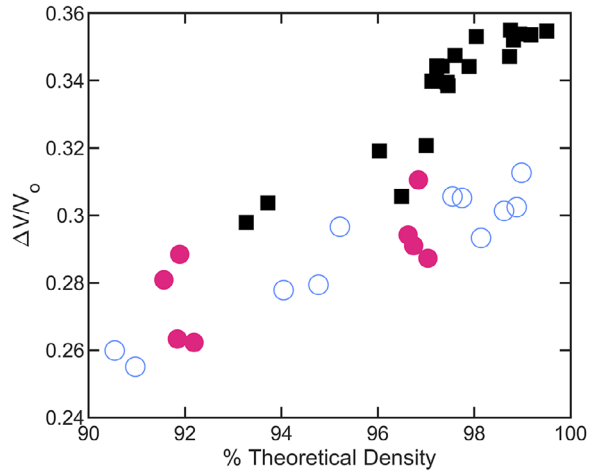

FIGURE 5 | Change in volume vs. percent theoretical (based on a value of 6.08 g/cm^3) density (Archimedes) following sintering of CeO_2/Al_2O_3 precursors (black squares) and $CeAlO_3$ precursors with single-step sintering procedures (filled pink circles) and multi-step sintering procedures (open blue circles). The ordinate, $\Delta V/V_o$, is calculated as $(V_o\text{-}V_f)/V_o$, where V_o is the initial volume after debinding and V_f is the final sintered volume (see Supporting Information for additional details).

the $CeAlO_3$ phase cracked and broke apart after reheating in oxidizing conditions due to the large volume expansion of the eutectoid reaction (see Figure S4). Cracking of the samples could be avoided by bypassing the temperature range where catastrophic expansion occurs. This process was accomplished by introducing dense samples to oxidizing conditions at temperatures above a critical threshold. The critical threshold determined from the data in Figure 3 was between 1250°C and 1350°C. Dense $CeAlO_3$ samples oxidized above 1350°C fully transformed to CeO_2/Al_2O_3 microstructures, maintained high theoretical densities, and showed no signs of producing macro- or micro-sized cracks. Whereas dense $CeAlO_3$ samples oxidized at or below 1250°C shattered into many pieces during the reoxidation process or developed large visible macro-sized cracks.

3.4 | Microstructure

3.4.1 | Single-Step Reactive Sintering Microstructures

Samples were sintered under a variety of heat treatments and processing atmospheres in an effort to optimize densities and preserve fine microstructures. The resultant densities of sintered samples and corresponding processing conditions are documented in Supporting Information.

As shown from the dilatometry data in Figure 2, the onset temperature for sintering of the CeO_2/Al_2O_3 samples is much lower than the onset for sintering of the $CeAlO_3$ precursor samples. As a result, the densities of the CeO_2/Al_2O_3 samples are higher than the $CeAlO_3$ precursor samples for similar sintering conditions. When comparing the CeO_2/Al_2O_3 precursor samples to $CeAlO_3$ precursor samples sintered to comparable densities (Archimedes) in Figure 5, the $CeAlO_3$ precursor samples undergo a smaller change in volume during sintering. These results show that high densities with improved reduction in sintering shrinkage can be achieved by using a $CeAlO_3$ precursor. The theoretical density of CeO_2 + 1/2Al_2O_3 compositions is 6.08 g/cm^3, and it is possible to achieve greater than 95% of the theoretical density using both CeO_2/Al_2O_3 and $CeAlO_3$ precursors (Figure 5).

It should be noted that the green densities of the $CeAlO_3$ samples were lower than those of the CeO_2/Al_2O_3 precursor samples (57.2% ± 0.6 vs. 62.3% ± 0.4, respectively). This difference can be partially attributed to the fact that the calcined and milled $CeAlO_3$ precursor powder was significantly coarser than the starting CeO_2 and Al_2O_3 powders (see Figure S3). In general, higher green densities (lower porosity in a pre-sintered sample) result in higher sintered densities. Better powder packing efficiency can improve green densities by decreasing the average initial pore size, and smaller pores are easier to remove during sintering. Better control of the starting particle size of the $CeAlO_3$ powder could promote higher green density packing and further exaggerate the difference between the volume contraction curves of the $CeAlO_3$ versus CeO_2/Al_2O_3 precursors.

The microstructures of $CeAlO_3$ and CeO_2/Al_2O_3 precursor samples sintered using a single-step process are shown in Figure 6. The samples sintered using the $CeAlO_3$ starting powder contain more visible porosity than the CeO_2/Al_2O_3 samples. Unlike CeO_2/Al_2O_3, the $CeAlO_3$ samples undergo a large volume expansion prior to sintering, as shown in the dilatometry data in Figure 2, resulting in the creation of larger pores prior to densification, and this porosity is more difficult to remove during the sintering stage, resulting in lower relative densities. Sintering at or above 1550°C resulted in exaggerated growth of the lath-like aluminum-rich phases, consistent with the identification of $CeAl_{11}O_{18}$ in the X-ray diffraction data.

3.4.2 | Multi-Step Reactive Sintering Microstructures

Analysis was conducted on samples that were sintered below and above the critical temperature of 1550°C. Samples were densified using two multi-step approaches: (1) samples were heated under reducing conditions and oxidized at isothermal dwell (Figure 3), and (2) samples were first densified under reducing conditions at a high sintering temperature and then oxidized at a lower isothermal dwell (Figure 4). An improvement in the densities of $CeAlO_3$ precursor samples was achieved by this second strategy. This multi-step method (Figures 4 and 5 open circles) achieves high densities and fine lamellar microstructures at the expense of a larger transient shrinkage (densification and phase transformation occur sequentially), with sintering shrinkage preceding the expansion driven by the phase transformation (Figure 4), as opposed to the concurrent approach in which sintering shrinkage and transformation-driven expansion partially offset one another, reducing the magnitude of the transient dimensional strain (Figure 3). The maximum density (Archimedes) achieved (Figure 5) for the single-step approach (1) was 97.0% of theoretical density (this sample was sintered at 1650°C in air for 2 h) while the maximum density achieved for the multi-step approach (2) was 99.0% of theoretical density (this sample was sintered at 1550°C for 2 h under argon, followed by a second step at 1450°C for 1 h in air). While comparable densities were nearly achievable for the single-step compared to multi-step processing routes,

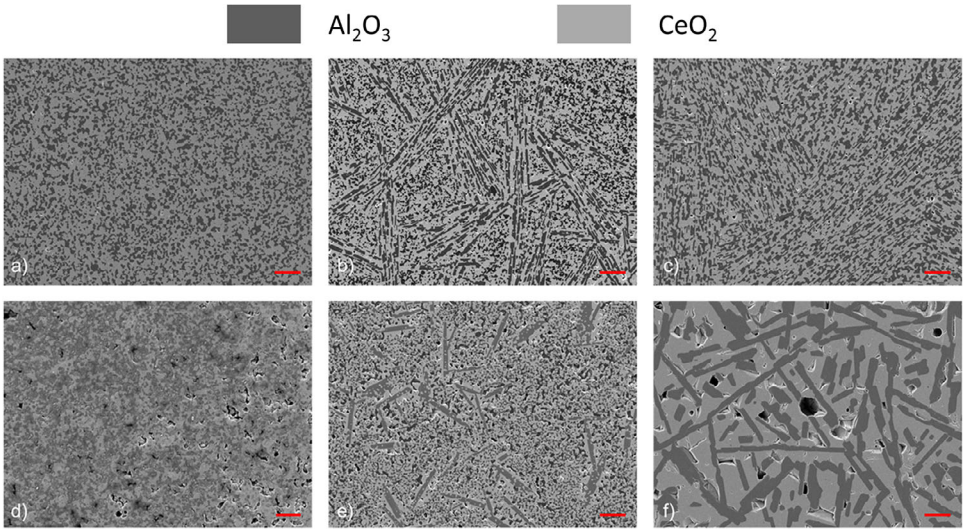

FIGURE 6 | Secondary electron images of polished cross sections of CeO_2/Al_2O_3 precursor samples sintered with a single-step process at (a) 1500°C for 16 h, (b) 1550°C for 2 h, and (c) 1650°C for 2 h, and $CeAlO_3$ precursor samples sintered with a single-step process at (d) 1500°C for 60 h, (e) 1550°C for 2 h, and (f) 1650°C for 20 h. Scale bars (red) are 10 μm.

there are significant differences in the resulting microstructures (see Figures 6f and 7c for examples of high-density single-step microstructure vs. Figures 7a and 8 for examples of high-density multi-step microstructure, as well as Supporting Information for additional examples).

As shown in Figure 7, samples with fine microstructural features sintered at or below 1550°C contain lamella of CeO_2 alternating mostly with α-Al_2O_3. Large-grained samples sintered above 1550°C exhibit equiaxed α-Al_2O_3 grains and large $CeAl_{11}O_{18}$ laths. For longer sintering times at higher temperatures, the $CeAl_{11}O_{18}$ platelet-like grains would continue to grow while the α-Al_2O_3 equiaxed grains would be consumed (see Figures S6–S8). A multi-step sintering procedure was adopted in an attempt to solve two issues that were evident form a single-step procedure; those issues being: (1) using a $CeAlO_3$ precursor, porosity was generated by the volume expansion of the eutectoid reaction compromising the final sintering densities, and (2) the time required to sinter samples to high density using a single-step procedure was long enough to produce significant coarsening of the microstructure. A multi-step processing route fixes both issues by allowing the sample to sinter to full density in the $CeAlO_3$ phase, followed by annealing in an oxidizing atmosphere only long enough to drive the eutectoid reaction to completion, resulting in minimal microstructural coarsening.

A wide range of reducing conditions was found to be sufficient for maintaining the $CeAlO_3$ phase to high temperatures. Unlike the calcination step where forming gas conditions were necessary to drive the eutectoid reaction, once formed, the $CeAlO_3$ phase could be stabilized in moderately reducing conditions maintained by flowing argon gas through the furnace. Using this multi-step process, the eutectoid decomposition proceeds quickly during the high temperature oxidation process, and the microstructure could be controlled by tuning the time/temperature conditions the sample was oxidized under. If samples were quenched during this step of the process, a fine, less than 100 nm lamellar microstructure could be preserved (Figure 8) similar to the microstructure produced in powder specimens in previously published results [32]. The resulting microstructural features are approximately an order of magnitude smaller than the initial particle size of precursor powders and smaller than the grain size of the $CeAlO_3$ sintered microstructure. These results suggest that the starting particle size or method for achieving high density of the initial $CeAlO_3$ sample has little effect on the final microstructure following the eutectoid decomposition, because the coarse-grained parent $CeAlO_3$ microstructure is replaced with CeO_2/Al_2O_3 lamella whose dimensions do not have a direct dependence on the parent microstructure.

3.5 | Hardness

Vickers microhardness measurements were made on cross sections of CeO_2/Al_2O_3 precursor samples densified using a multi-step sintering process (these samples, for clarity, will be referred to as partially and fully reacted samples going forward). The partially reacted sample was sintered at 1550°C for 12 h in forming gas (this step transforms the precursors to $CeAlO_3$ and densifies the powder in the perovskite phase), followed by oxidation at 1600°C for 10 min with subsequent quenching of the sample. This sample was mostly reoxidized to form CeO_2/Al_2O_3 lamellar microstructure with a small unreacted $CeAlO_3$ core. The surface of the sample oxidized first, and this reaction front moves inward, resulting in more pronounced coarsening of the microstructure toward the surface of the sample. The fully reacted sample was sintered at 1550°C for 12 h in forming gas, followed by oxidation at 1550°C for 30 min with subsequent quenching of the sample. An evenly spaced grid of 348 indentations was made on each sample, and the lamellar spacings in the vicinity of these microhardness indentations were measured from SEM images. The variability of the lamellar coarsening from the sample surface to the inner core of these two samples can be observed in Figure 8. Representative measurements of the lamellar spacing distributions around these indentations are shown in Figure 9a. As shown in Figure 9b, the partially reacted sample exhibits a hardness gradient increasing in

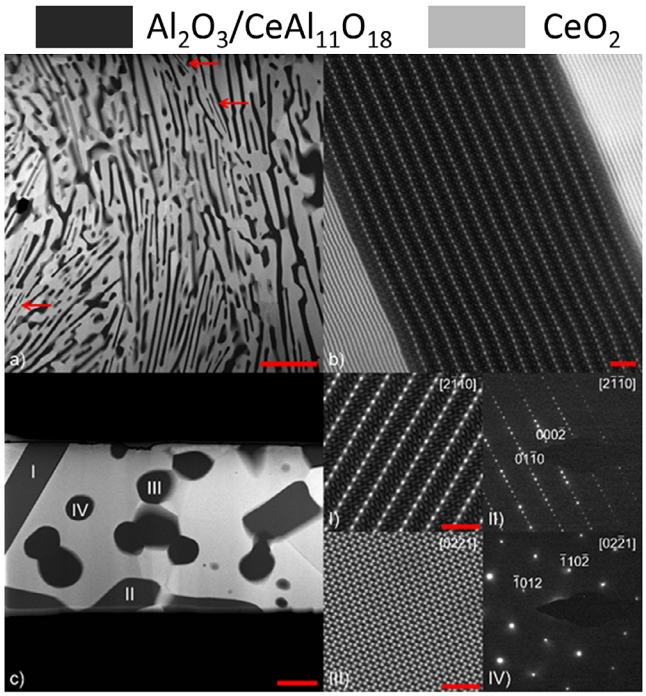

FIGURE 7 | A region from the approximate center of an oxidized $CeAlO_3$ precursor pellet (a). It was sintered with a multi-step process at 1550°C for 12 h prior to oxidizing the sample for 10 min at 1550°C in air followed by quenching. While some coarsening is evident, lamella of alternating layers of α-Al_2O_3 and CeO_2 are present (a). In addition to α-Al_2O_3, $CeAl_{11}O_{18}$ was also identified using atomic resolution imaging (b) and electron diffraction (not shown). These $CeAl_{11}O_{18}$ features tended to be smaller than the α-Al_2O_3 and examples are illustrated with red arrows in (a). In a $CeAlO_3$ precursor pellet sintered with a single-step process at 1600°C for 2 h, the microstructure consisted of platelet and spherical grains interspersed with the cerium dioxide grains (c). Atomic resolution imaging and selected area diffraction indicates the platelets are $CeAl_{11}O_{18}$ while the spherical grains are α-Al_2O_3. Examples of the $CeAl_{11}O_{18}$ (I, II) and α-Al_2O_3 (III, IV) are indicated. Scale bars are equal to 1 μm (a, c) and 2 nm (b, I, III).

value from the surface toward the unreacted core. The eutectoid reaction requires oxygen to progress, and a diffusion gradient is evident with the surface reacting first and having more time to coarsen. The unreacted $CeAlO_3$ core is much softer than the CeO_2/Al_2O_3 composite microstructure shell, and a sharp drop-off in hardness is measured in this region. The fully reacted sample has a more homogeneous microstructure at the expense of lamella coarsening to dimensions greater than the sub-100 nm features present in the partially reacted sample. The sizes of the lamellar spacings show good correlation with hardness and follow a Hall–Petch trend (Figure 9c).

Ideally, the thermal/oxidation processing cycles would be tuned for a particular sample according to its geometric dimensions to form a microstructure optimized for a particular application, and the kinetics of the eutectoid reaction and resulting coarsening may be further improved by manipulating the oxygen partial pressure during reoxidation (see Figure S1). However, samples with distributions of microstructural features do not necessarily provide a detriment to improving combinations of strength and toughness, because strength improvements and crack growth modifications can occur at different length scales [56]. In fact, hierarchical composite materials with broad microstructural length scales often exhibit enhanced toughness [57], and microstructures with layered or high-aspect ratio inclusions can lead to enhanced mechanical properties [58]. While the transformation of Al_2O_3 to $CeAl_{11}O_{18}$ coincides with coarsening of the microstructure, examples of similar coarse-grained hexaaluminate phases leading to improved toughness have been reported [49, 50, 53, 59, 60]. Composites with hierarchical microstructural features can combine weak and strong interfaces with compliant and hard phases that act together to deflect cracks through a multitude of energy-dissipative mechanisms [61]. As shown in Figure 8, there is evidence from the structure of the cracks emanating from the microhardness indentations that possible toughening mechanisms are active in these samples. Example SEM micrographs highlight crack branching (multiple cracks being formed and branching out from a parent crack), crack bridging (discontinuities in the crack), and crack deflection (instances where the crack will migrate around the perimeter of an alumina lamellar inclusion rather than pass through it—see Figure S11 for additional examples). Future work will be required to confirm the relationship between these nano-lamellar microstructures and improved mechanical properties, and should focus on measurements of quantitative toughness values like K_{IC}.

4 | Discussion

Successful consolidation of CeO_2/Al_2O_3 phases into a dense, low-porosity sintered body using a reactive sintering route could potentially solve multiple ceramic engineering challenges. These challenges include reducing the amount of net shrinkage from green-body to dense part, preservation of nanostructure in the sintered part, and a reduction of heating cycles/processing steps. For materials in critical applications like medical implants or structural components, combining small grain or microstructural feature sizes with additional toughening mechanisms is essential. Nanoceramics offer promise for these industries by providing high densities of crack-impeding features that improve mechanical properties compared to ceramics with non-nano-sized microstructural features [62, 63].

When sintered to near theoretical density in the perovskite $CeAlO_3$ phase, reoxidation is diffusion controlled from the surface of the sample to the inner core, and partially reacted samples containing oxidized CeO_2/Al_2O_3 shells with unreacted $CeAlO_3$ cores were prone to form large cracks through the $CeAlO_3$ phase (see Figure S4). For samples that were processed under nearly identical conditions (for example, samples were sintered to nearly full density under reducing conditions in the $CeAlO_3$ phase then oxidized to form CeO_2/Al_2O_3 at temperatures of 1550°C followed by quenching), crack formation was only present in samples with residual unreacted $CeAlO_3$ phase (see Figure S9). These observations suggest that this type of cracking was formed during cooling by differences in thermal expansion coefficient between the perovskite and CeO_2/Al_2O_3 composite phases; otherwise, if cracks were formed during the rapid volume expansion of the eutectoid oxidation step, observation of cracks would be expected in both partially and fully reacted samples. It should be noted that crack formation, when observed, was always catastrophic and penetrated through the surface of the pellet, making it

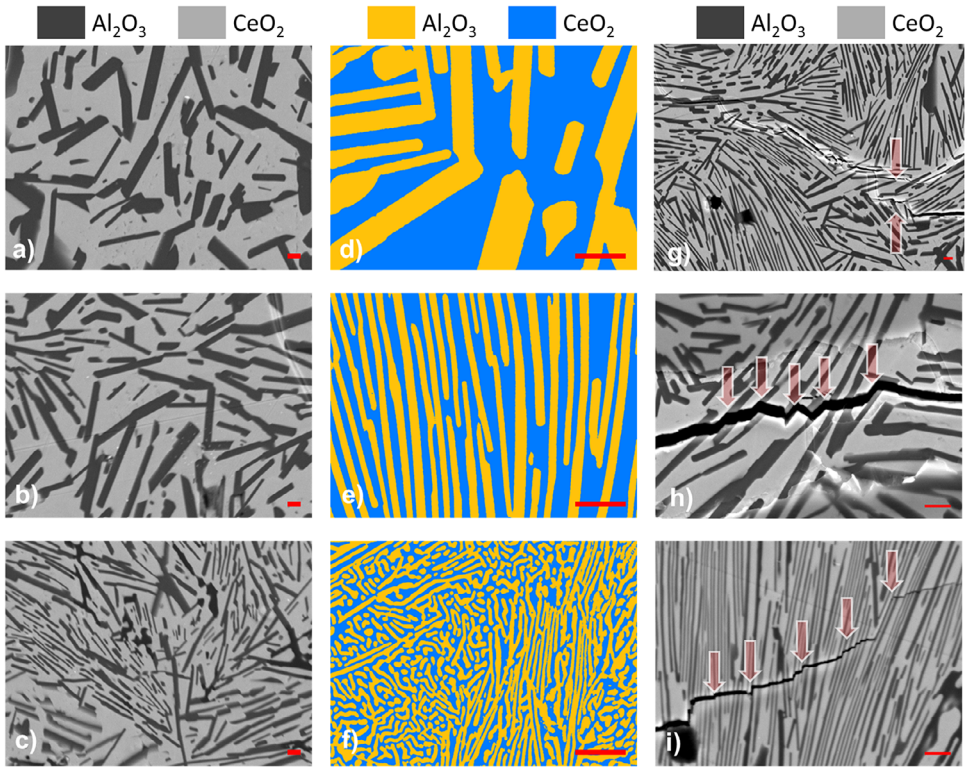

FIGURE 8 | (a–c) Secondary electron images of fully reacted $CeAlO_3$ precursor sample microstructures sintered with a multi-step process moving from hardness tested regions closest to the sample surface (top row) toward the core (bottom row), (d–f) segmented images of partially reacted sample microstructures moving from hardness tested regions closest to the sample surface (top row) toward the core (bottom row), and (g–i) selected images of cracking emanating from the indentation with highlighted critical points (arrows) for g) crack branching and (h, i) crack bridging, The scale bar (red) for all images is 500 nm.

easily identifiable. Crack formation was observed in samples with residual $CeAlO_3$ mixed with CeO_2/Al_2O_3 phases, and more work is needed to determine the responsible mechanisms (displacive phase transitions occur in the $CeAlO_3$ phases around 1100°C) and any possible relationship between them and thermal expansion mismatch. Cracking of samples also occurred if samples of dense $CeAlO_3$ were heated slowly in oxidizing conditions from room temperature to eutectoid phase transition onset temperatures.

Fast heating or fast oxidation (heating the sample in reducing conditions above the eutectoid onset temperature followed by oxidation) consistently created conditions that avoided crack formation. The optimized quenching rate and quench temperature were not identified in this study, as the purpose of quenching the samples was to arrest the coarsening mechanisms and preserve the finest CeO_2/Al_2O_3 microstructure possible. Additional work will be required to elucidate the relationship between cooling rate, lamellar size distribution, and the formation of cracks. It is presumed that the kinetics of the eutectoid phase transformation depend heavily on the oxygen transport kinetics in the reactant and product phases, and doping strategies should be employed to adjust the rate of oxidation to optimize the resulting microstructure and minimize processing-related defects.

At high temperatures, multiple thermally activated mass transport mechanisms related to surface, bulk, and grain boundary diffusion are competing for dominance [64] over point defect formation, densification, and coarsening mechanisms [65]. At sufficient temperatures, ceramics can undergo a transition that promotes metallic-like creep (superplasticity) at high strain and strain rates while avoiding the formation of defects or critical necking [66]. For superplasticity in ceramics, two conditions must be met: small grain size and a processing temperature greater than half the melting temperature ($0.5T_m$) [67]. In the CeO_2/Al_2O_3 composite system, the melting points of the oxides are 1973°C and 2072°C, respectively. By utilizing a multi-step reaction process and initiating the eutectoid decomposition at temperatures above 0.5 T_m, it could be speculated that the large strains induced by the eutectoid volume expansion are accommodated by a grain-boundary sliding mechanism typical of superplasticity or high-temperature creep, allowing for the production of crack-free samples. Superplasticity has been attributed to the accommodation of large strains in ceramic composite materials [68] as well as the mechanism for facilitating fast densification rates in novel sintering methods [69]. These novel sintering methods rely on ultra-fast heating and cooling and include spark plasma [70], black-light [71], and ultrafast high-temperature sintering [72]. The nanoceramic CeO_2/Al_2O_3 composite exhibits improved densities with finer microstructural features, leading to improved strength when processed with fast eutectoid reaction kinetics at elevated temperatures, and refinement of the microstructure could be further achieved with more control over rapid heating and cooling rates. Additionally, the degree of volume expansion during the eutectoid reaction can be significantly reduced with

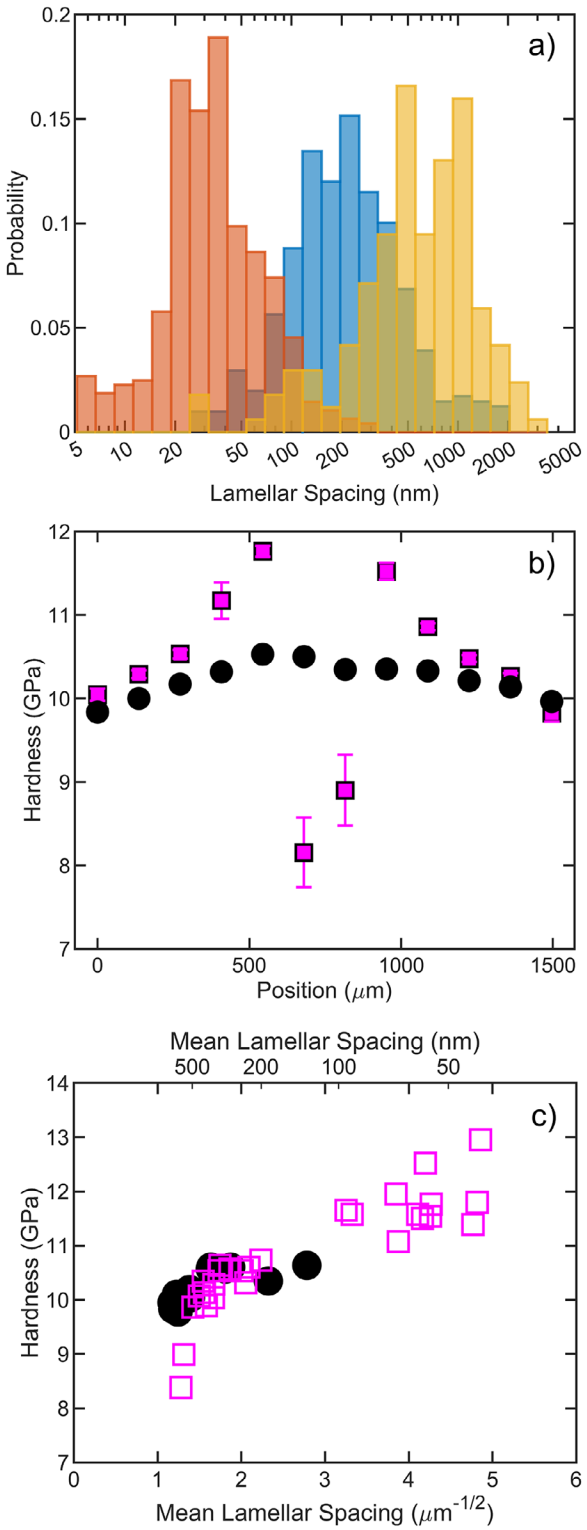

FIGURE 9 | Hardness results with (a) histogram plots of lamellar spacings for different regions (see Figure S10–S14 for additional details) of partially reacted samples for regions: near-surface (yellow), near-reaction front (red), and the area in between these two locations (blue), (b) the mean hardness values of a partially (pink squares) and fully reacted (black circles) sample cross section (error bars are a single standard deviation from the mean of 29 hardness values), and (c) the hardness values vs. interlamellar spacing for both a partially reacted (pink squares) and fully reacted (black circles) sample plotted on an inverse square root scale abscissa to allow for a visual inspection of a Hall–Petch trend.

different choices of chemical substitution or alloying on the Ce^{3+} or Al^{3+} sites. The perovskite phase is compliant to chemical substitution, and this feature opens the phase diagram to a wide variety of potential compositions.

5 | Conclusions

A novel route to producing dense CeO_2/Al_2O_3 ceramic/ceramic composite microstructures was developed. A reduction in shrinkage during sintering can be achieved by performing a reactive sintering procedure, transforming $CeAlO_3$ to a larger molar volume CeO_2/Al_2O_3 composite microstructure. The production of dense CeO_2/Al_2O_3 microstructures using a $CeAlO_3$ reactant is beneficial in that the eutectoid decomposition is driven by a redox reaction. This additional tunable processing parameter, oxygen activity, adds another lever of control over the microstructural development and kinetics. A multi-step heating/oxidation method, exploiting this additional degree of processing control, facilitates the formation of microstructures with sub-100 nm scale features in dense, relatively pore-free samples. The hardness of these composite microstructures was inversely proportional to lamellar spacing and qualitative improvements in crack deflection were inferred from microstructural images in samples with fine lamellar features. Therefore, judicious control of the thermal history of the samples is important to stymy thermally induced microstructural coarsening and control the final feature size.

Acknowledgments

Aspects of this manuscript are included in a currently pending patent: Near Net Shape Densification of Cerium Composites and Making Nano-Sized Phase-Separated Microstructures in Ceramics, Patent Application # PCT/US25/39858.

Funding

The authors have nothing to report.

Disclaimer

Certain commercial equipment, instruments, or materials are identified in this paper in order to specify the experimental procedure adequately. Such identification is not intended to imply recommendation or endorsement by the National Institute of Standards and Technology, nor is it intended to imply that the materials or equipment identified are necessarily the best available for the purpose.

Conflicts of Interest

The authors declare no conflicts of interest.

References

1. M. N. Rahaman, "Kinetics and Mechanisms of densification," in *Sintering of Advanced Materials*, ed. Z. Z. Fang (Woodhead Publishing, 2010), 33–64, https://doi.org/10.1533/9781845699949.1.33.

2. J. D. Kuntz, G.-D. Zhan, and A. K. Mukherjee, "Nanocrystalline-Matrix Ceramic Composites for Improved Fracture Toughness," *MRS Bulletin* 29 (2004): 22–27.

3. R. K. Bordia, S. J. L. Kang, and E. A. Olevsky, "Current Understanding and Future Research Directions at the Onset of the Next Century of

Sintering Science and Technology," *Journal of the American Ceramic Society* 100 (2017): 2314–2352, https://doi.org/10.1111/jace.14919.

4. P. Greil, "Near Net Shape Manufacturing of Polymer Derived Ceramics," *Key Engineering Materials* 132–136 (1997): 1981–1984, https://doi.org/10.4028/www.scientific.net/kem.132-136.1981.

5. P. Greil, "Near Net Shape Manufacturing of Ceramics," *Materials Chemistry and Physics* 61 (1999): 64–68, https://doi.org/10.1016/S0254-0584(99)00115-7.

6. W. G. Fahrenholtz, K. G. Ewsuk, D. T. Ellerby, and R. E. Loehman, "Near-Net-Shape Processing of Metal-Ceramic Composites by Reactive Metal Penetration," *Journal of the American Ceramic Society* 79 (1996): 2497–2499, https://doi.org/10.1111/j.1151-2916.1996.tb09005.x.

7. L. Wang and F. Aldinger, "Near-Net Shape Forming of Advanced Ceramics," *Advanced Engineering Materials* 2 (2000): 110–113, https://doi.org/10.1002/(SICI)1527-2648(200003)2:3⟨110::AID-ADEM110⟩3.0.CO;2-4.

8. M. J. Mayo, "Processing of Nanocrystalline Ceramics From Ultrafine Particles," *International Materials Reviews* 41 (1996): 85–115, https://doi.org/10.1179/imr.1996.41.3.85.

9. B. Ratzker, A. Wagner, M. Sokol, L. Meshi, S. Kalabukhov, and N. Frage, "Deformation in Nanocrystalline Ceramics: A Microstructural Study of $MgAl_2O_4$," *Acta Materialia* 183 (2020): 137–144, https://doi.org/10.1016/j.actamat.2019.11.015.

10. A. Mukhopadhyay and B. Basu, "Consolidation-Microstructure-Property Relationships in Bulk Nanoceramics and Ceramic Nanocomposites: A Review," *International Materials Reviews* 52 (2007): 257–288, https://doi.org/10.1179/174328007X160281.

11. H. Ryou, J. W. Drazin, K. J. Wahl, et al., "Below the Hall-Petch Limit in Nanocrystalline Ceramics," *ACS Nano* 12 (2018): 3083–3094, https://doi.org/10.1021/acsnano.7b07380.

12. D. Damjanovic, "Ferroelectric, Dielectric and Piezoelectric Properties of Ferroelectric Thin Films and Ceramics," *Reports on Progress in Physics* 61 (1998): 1267–1324, https://doi.org/10.1088/0034-4885/61/9/002.

13. W. Ming, Z. Jiang, G. Luo, et al., "Progress in Transparent Nano-Ceramics and Their Potential Applications," *Nanomaterials* 12 (2022): 1491, https://doi.org/10.3390/nano12091491.

14. Z. Chen, X. Zhang, and Y. Pei, "Manipulation of Phonon Transport in Thermoelectrics," *Advanced Materials* 30 (2018): 1–12, https://doi.org/10.1002/adma.201705617.

15. M. A. Meyers, A. Mishra, and D. J. Benson, "Mechanical Properties of Nanocrystalline Materials," *Progress in Materials Science* 51 (2006): 427–556, https://doi.org/10.1016/j.pmatsci.2005.08.003.

16. R. M. German, "Prediction of Packing and Sintering Density for Bimodal Powder Mixtures," *Advances in Powder Metallurgy* 3 (1992): 1–15, https://doi.org/10.1016/0026-0657(93)92034-3.

17. T.-S. Yeh and M. D. Sacks, "Effect of Particle Size Distribution on the Sintering of Alumina," *Journal of the American Ceramic Society* 71 (1988): C-484–C-487, https://doi.org/10.1111/j.1151-2916.1988.tb05812.x.

18. R. M. German, P. Suri, and S. J. Park, "Review: Liquid Phase Sintering," *Journal of Materials Science* 44 (2009): 1–39, https://doi.org/10.1007/s10853-008-3008-0.

19. N. Claussen, T. Le, and S. Wu, "Low-Shrinkage Reaction-Bonded Alumina," *Journal of the European Ceramic Society* 5 (1989): 29–35, https://doi.org/10.1016/0955-2219(89)90006-X.

20. N. Claussen, N. A. Travitzky, and S. Wu, "Tailoring of Reaction-Bonded Al_2O_3 (RBAO) Ceramics," in *A Collection of Papers Presented at the 14th Annual Conference on Composites and Advanced Ceramic Materials: Ceramic Engineering and Science Proceedings*, ed. J. B. Wachtman Jr. (The American Ceramic Society Inc., 1990), 806–820, https://doi.org/10.1002/9780470313008.ch22.

21. D. Yao, C. M. Gomes, Y.-P. Zeng, D. Jiang, J. Günster, and J. G. Heinrich, "Near Zero Shrinkage Porous Al_2O_3 Prepared via 3D-Printing and Reaction Bonding," *Materials Letters* 147 (2015): 116–118, https://doi.org/10.1016/j.matlet.2015.02.037.

22. Y. Dong, H. Yang, L. Zhang, et al., "Ultra-Uniform Nanocrystalline Materials via Two-Step Sintering," *Advanced Functional Materials* 31 (2021): 2007750, https://doi.org/10.1002/adfm.202007750.

23. K. J. Wynne and R. W. Rice, "Ceramics via Polymer Pyrolysisdagger," *Annual Review of Materials Science* 14 (1984): 297–334, https://doi.org/10.1146/annurev.ms.14.080184.001501.

24. P. Greil, "Active-Filler-Controlled Pyrolysis of Preceramic Polymers," *Journal of the American Ceramic Society* 78 (1995): 835–848, https://doi.org/10.1111/j.1151-2916.1995.tb08404.x.

25. A. W. Urquhart, "Novel Reinforced Ceramics and Metals: A Review of Lanxide's Composite Technologies," *Materials Science and Engineering A* 144 (1991): 75–82, https://doi.org/10.1016/0921-5093(91)90211-5.

26. W. Hong, L. C. De Jonghe, X. Yang, and M. N. Rahaman, "Reaction Sintering of ZnO-AI_2O_3," *Journal of the American Ceramic Society* 78 (1995): 3217–3224, https://doi.org/10.1111/j.1151-2916.1995.tb07957.x.

27. A. Trovarelli, "Catalytic Properties of Ceria and CeO_2-Containing Materials," *Catalysis Reviews* 38 (1996): 439–520, https://doi.org/10.1080/01614949608006464.

28. N. A. Piro, J. R. Robinson, P. J. Walsh, and E. J. Schelter, "The Electrochemical Behavior of Cerium(III/IV) Complexes: Thermodynamics, Kinetics and Applications in Synthesis," *Coordination Chemistry Reviews* 260 (2014): 21–36, https://doi.org/10.1016/j.ccr.2013.08.034.

29. D. J. M. Bevan and J. Kordis, "Mixed Oxides of the Type MO_2 (Fluorite)—M_2O_3—I Oxygen Dissociation Pressures and Phase Relationships in the System CeO_2 Ce_2O_3 at High Temperatures," *Journal of Inorganic and Nuclear Chemistry* 26 (1964): 1509–1523, https://doi.org/10.1016/0022-1902(64)80038-5.

30. R. Schmitt, A. Nenning, O. Kraynis, et al., "A Review of Defect Structure and Chemistry in Ceria and Its Solid Solutions," *Chemical Society Reviews* 49 (2020): 554–592, https://doi.org/10.1039/c9cs00588a.

31. D. A. Andersson, S. I. Simak, B. Johansson, I. A. Abrikosov, and N. V. Skorodumova, "Modeling of CeO_2, Ce_2O_3, and CeO_2-x in the LDA + U Formalism," *Physical Review B—Condensed Matter and Materials Physics* 75 (2007): 035109, https://doi.org/10.1103/PhysRevB.75.035109.

32. A. C. Johnston-Peck and R. A. Maier, "Eutectoid Decompositions in Ce-Containing ABO_3 Perovskites: Part I, the Case of Cooperative Growth in $CeAlO_3$," *Journal of the American Ceramic Society* (2023): 2765–2775, https://doi.org/10.1111/jace.19595.

33. A. C. Johnston-Peck, A. J. Biacchi, and R. A. Maier, "Eutectoid Decompositions in Ce-Containing ABO_3 Perovskites: Part II, the Case of Divorced Growth in $CeCrO_3$," *Journal of the American Ceramic Society* 107 (2024): 2765–2775, https://doi.org/10.1111/jace.19773.

34. P. Wu and A. D. Pelton, "Coupled Thermodynamic-Phase Diagram Assessment of the Rare Earth Oxide-Aluminium Oxide Binary Systems," *Journal of Alloys and Compounds* 179 (1992): 259–287, https://doi.org/10.1016/0925-8388(92)90227-Z.

35. M. Mizuno, R. Berjoan, J.-P. Coutures, and M. Foex, "Phase Diagram of the System Al_2O_3-CeO_2 at Liquidus Temperature," *Journal of the Ceramic Association of Japan* 83 (1975): 90–96, https://doi.org/10.2109/jcersj1950.83.954_90.

36. M. Guizar-Sicairos, S. T. Thurman, and J. R. Fienup, "Efficient Subpixel Image Registration Algorithms," *Optics Letters* 33 (2008): 156, https://doi.org/10.1364/ol.33.000156.

37. J. Schindelin, I. Arganda-Carreras, E. Frise, et al., "Fiji: An Open-Source Platform for Biological-image Analysis," *Nature Methods* 9 (2012): 676–682, https://doi.org/10.1038/nmeth.2019.

38. E. Frank, M. A. Hall, and I. H. Witten, The WEKA Workbench: *Online Appendix for "Data Mining: Practical Machine Learning Tools and Techniques"* (Morgan Kaufmann, 2016), https://ml.cms.waikato.ac.nz/weka/Witten_et_al_2016_appendix.pdf.

39. N. Doebelin and R. Kleeberg, "Profex : A Graphical User Interface for the Rietveld Refinement Program BGMN," *Journal of Applied Crystallography* 48 (2015): 1573–1580, https://doi.org/10.1107/S1600576715014685.

40. A. Feteira, D. C. Sinclair, and M. T. Lanagan, "Structural and Electrical Characterization of $CeAlO_3$ Ceramics," *Journal of Applied Physics* 101 (2007): 064110, https://doi.org/10.1063/1.2559648.

41. K. Tsukuma, "Conversion From β-Ce_2O_3 $11Al_2O_3$ to α-Al_2O_3 in Tetragonal ZrO_2 Matrix," *Journal of the American Ceramic Society* 83 (2000): 3219–3221, https://doi.org/10.1111/j.1151-2916.2000.tb01711.x.

42. S. Shi, S. Cho, T. Goto, and T. Sekino, "Role of $CeAl_{11}O_{18}$ in Reinforcing Al_2O_3/Ti Composites by Adding CeO_2," *International Journal of Applied Ceramic Technology* 18 (2021): 170–181, https://doi.org/10.1111/ijac.13629.

43. A. C. Tas and M. Akinc, "Phase Relations in the System Ce_2O_3–Al_2O_3 in Inert and Reducing Atmospheres," *Journal of the American Ceramic Society* 77 (1994): 2961–2967, https://doi.org/10.1111/j.1151-2916.1994.tb04531.x.

44. S. M. Naga, H. F. El-Maghraby, M. Awaad, F. Kern, R. Gadow, and A. M. Hassan, "Preparation and Characterization of Tough Cerium Hexaaluminate Bodies," *Materials Letters* 254 (2019): 402–406, https://doi.org/10.1016/j.matlet.2019.07.116.

45. I. Akin, E. Yilmaz, F. Sahin, O. Yucel, and G. Goller, "Effect of CeO_2 Addition on Densification and Microstructure of Al_2O_3-YSZ Composites," *Ceramics International* 37 (2011): 3273–3280, https://doi.org/10.1016/j.ceramint.2011.05.123.

46. Y. Q. Wu, Y. F. Zhang, X. X. Huang, and J. K. Guo, "In-Situ Growth of Needlelike $LaAl_{11}O_{18}$ for Reinforcement of Alumina Composites," *Ceramics International* 27 (2001): 903–906, https://doi.org/10.1016/S0272-8842(01)00044-X.

47. F. Kern, "Structure-Property Relations in Alumina-Zirconia Nanocomposites Reinforced With In Situ Formed Cerium Hexaaluminate Precipitates," *Scripta Materialia* 67 (2012): 1007–1010, https://doi.org/10.1016/j.scriptamat.2012.09.019.

48. F. Kern, "Effect of In Situ-Formed Cerium Hexaaluminate Precipitates on Properties of Alumina -24vol% Zirconia (1.4Y) Composites," *Journal of Ceramic Science and Technology* 4 (2013): 177–186, https://doi.org/10.4416/JCST2013-00014.

49. S. M. Naga, A. M. Hassan, H. F. El-Maghraby, M. Awaad, and H. Elsayed, "In-Situ Sintering Reaction of Al_2O_3-$LaAl_{11}O_{18}$-ZrO_2 Composite," *International Journal of Refractory Metals and Hard Materials* 54 (2016): 230–236, https://doi.org/10.1016/j.ijrmhm.2015.07.026.

50. P. Chen and I. Chen, "In-Situ Alumina/Aluminate Platelet Composites," *Journal of the American Ceramic Society* 75 (1992): 2610–2612, https://doi.org/10.1111/j.1151-2916.1992.tb05623.x.

51. N. A. Rejab, A. Z. A. Azhar, M. M. Ratnam, and Z. A. Ahmad, "The Relationship Between Microstructure and Fracture Toughness of Zirconia Toughened Alumina (ZTA) Added With MgO and CeO_2," *International Journal of Refractory Metals and Hard Materials* 41 (2013): 522–530, https://doi.org/10.1016/j.ijrmhm.2013.07.002.

52. J. Chevalier, A. Liens, H. Reveron, et al., "Forty Years After the Promise of "Ceramic Steel?": Zirconia-Based Composites With a Metal-Like Mechanical Behavior," *Journal of the American Ceramic Society* 103 (2020): 1482–1513, https://doi.org/10.1111/jace.16903.

53. M. Fornabaio, P. Palmero, R. Traverso, et al., "Zirconia-Based Composites for Biomedical Applications: Role of Second Phases on Composition, Microstructure and Zirconia Transformability," *Journal of the European Ceramic Society* 35 (2015): 4039–4049, https://doi.org/10.1016/j.jeurceramsoc.2015.04.027.

54. B. J. McEntire, B. S. Bal, M. N. Rahaman, J. Chevalier, and G. Pezzotti, "Ceramics and Ceramic Coatings in Orthopaedics," *Journal of the European Ceramic Society* 35 (2015): 4327–4369, https://doi.org/10.1016/j.jeurceramsoc.2015.07.034.

55. I. Levin and D. Brandon, "Metastable Alumina Polymorphs: Crystal Structures and Transition Sequences," *Journal of the American Ceramic Society* 81 (1998): 1995–2012, https://doi.org/10.1111/j.1151-2916.1998.tb02581.x.

56. S. Kumar and H. Le Ferrand, "Nacre-Like Ceramic–Metal Composites: State-of-the-Art, Challenges, and Opportunities," *Journal of the American Ceramic Society* 108 (2025): e20623, https://doi.org/10.1111/jace.20623.

57. M. Mirkhalaf, A. K. Dastjerdi, and F. Barthelat, "Overcoming the Brittleness of Glass Through Bio-Inspiration and Micro-Architecture," *Nature Communications* 5 (2014): 3166, https://doi.org/10.1038/ncomms4166.

58. H. M. Chan, "Layered Ceramics: Processing and Mechanical Behavior," *Annual Review of Materials Science* 27 (1997): 249–282, https://doi.org/10.1146/annurev.matsci.27.1.249.

59. Z. D. I. Sktani, A. Z. A. Azhar, M. M. Ratnam, and Z. A. Ahmad, "The Influence of In-Situ Formation of Hibonite on the Properties of Zirconia Toughened Alumina (ZTA) Composites," *Ceramics International* 40 (2014): 6211–6217, https://doi.org/10.1016/j.ceramint.2013.11.076.

60. S. Sarker, H. T. Mumu, M. Al-Amin, M. Zahangir Alam, and M. A. Gafur, "Impacts of Inclusion of Additives on Physical, Microstructural, and Mechanical Properties of Alumina and Zirconia Toughened Alumina (ZTA) Ceramic Composite: A Review," *Materials Today: Proceedings* 62 (2022): 2892–2918, https://doi.org/10.1016/j.matpr.2022.02.481.

61. H. L. Gao, S. M. Chen, L. B. Mao, et al., "Mass Production of Bulk Artificial Nacre With Excellent Mechanical Properties," *Nature Communications* 8 (2017): 287, https://doi.org/10.1038/s41467-017-00392-z.

62. T. Ohji, Y. K. Jeong, Y. H. Choa, and K. Niihara, "Strengthening and Toughening Mechanisms of Ceramic Nanocomposites," *Journal of the American Ceramic Society* 81 (1998): 1453–1460, https://doi.org/10.1111/j.1151-2916.1998.tb02503.x.

63. P. Benetti, J. R. Kelly, and A. D. Bona, "Analysis of Thermal Distributions in Veneered Zirconia and Metal Restorations During Firing," *Dental Materials* 29 (2013): 1166–1172, https://doi.org/10.1016/j.dental.2013.08.212.

64. R. L. Coble, "Initial Sintering of Alumina and Hematite," *Journal of the American Ceramic Society* 41 (1958): 55–62, https://doi.org/10.1111/j.1151-2916.1958.tb13519.x.

65. M. F. Ashby, "A First Report on Sintering Diagrams," *Acta Metallurgica* 22 (1974): 275–289, https://doi.org/10.1016/0001-6160(74)90167-9.

66. T. G. Langdon, "Seventy-Five Years of Superplasticity: Historic Developments and New Opportunities," *Journal of Materials Science* 44 (2009): 5998–6010, https://doi.org/10.1007/s10853-009-3780-5.

67. Y. Maehara and T. G. Langdon, "Superplasticity in Ceramics," *Journal of Materials Science* 25 (1990): 2275–2286, https://doi.org/10.1007/BF00638018.

68. B.-N. Kim, K. Hiraga, K. Morita, and Y. Sakka, "A High-Strain-Rate Superplastic Ceramic," *Nature* 413 (2001): 288–291, https://doi.org/10.1038/35095025.

69. Y. Shan, X. Li, W. Zhao, et al., "Programmable and Rapid Fabrication of Complex-Shape Ceramics," *Nature Communications* 15 (2024): 9973, https://doi.org/10.1038/s41467-024-54393-w.

70. O. Guillon, W. Rheinheimer, and M. Bram, "A Perspective on Emerging and Future Sintering Technologies of Ceramic Materials," *Advanced Engineering Materials* 25 (2023): 2201870, https://doi.org/10.1002/adem.202201870.

71. L. Porz, M. Scherer, D. Huhn, et al., "Blacklight Sintering of Ceramics," *Materials Horizons* 9 (2022): 1717–1726, https://doi.org/10.1039/d2mh00177b.

72. C. Wang, W. Ping, Q. Bai, et al., "A General Method to Synthesize and Sinter Bulk Ceramics in Seconds," *Science* 368 (2020): 521–526, https://doi.org/10.1126/science.aaz7681.

Supporting Information

Additional supporting information can be found online in the Supporting Information section.

Supporting File 1: jace70752-sup-0001-SupMat.pdf.

Supporting File 2: jace70752-sup-0002-SupMat.xlsx.